In this case, an expression for d^2y/dx^2 is needed because it appears in Eq. (28). Equation (26) is differentiated a second time with respect to x to determine d^2y/dx^2. Before proceeding with this differentiation, some additional intermediate variables are defined to simplify the results of the differentiation

$$D \doteq 2ad(1/b), \qquad E \doteq 2ad \tag{29}$$

The expression for d^2y/dx^2 is quite lengthy but consists of two terms in the numerator and a squared expression in the denominator:

$$\frac{d^2y}{dx^2} = \frac{FG - HI}{J^2} \tag{30}$$

The first factor F is

$$F = Exy(1+ay^2)^{d-1} - (1/b)(1+ax^2)^d \tag{31}$$

This expression goes to $-1/b$ as x and y go to zero. The second factor G is

$$G = Dxy(d-1)(1+ax^2)^{d-2}2ax + (1+ax^2)^{d-1}D\left(x\frac{dy}{dx}+y\right) - d(1+ay^2)^{d-1}2ya\frac{dy}{dx} \tag{32}$$

The value of all terms in this expression go to zero as x and y go to zero. Thus, the product FG goes to zero as x goes to zero. The factor H in Eq. (30) is

$$H = Dxy(1+ax^2)^{d-1} - (1+ay^2)^d \tag{33}$$

In this case, as x and y go to zero, the value of this expression goes to -1. Factor I in Eq. (30) is

$$I = Exy(d-1)(1+ay^2)^{d-2}2ay\frac{dy}{dx} + (1+ay^2)^{d-1}E\left(x\frac{dy}{dx}+y\right) - d\frac{1}{b}(1+ax^2)^{d-1}2xa \tag{34}$$

The value of this expression becomes zero as x and y go to zero. Thus, the limit of HI is zero. Therefore, the limit of the numerator of Eq. (30) $[FG - HI]$ is zero. The denominator is

$$J^2 = [Exy(1+ay^2)^{d-1} - (1/b)(1+ax^2)^d]^2 \tag{35}$$

The limiting value of this expression as x and y go to zero is $(-1/b)^2$. However, because the numerator is zero, therefore,

$$\lim_{x\Rightarrow 0}\frac{d^2y}{dx^2} = \frac{-1/b\cdot 0 - (-1)\cdot 0}{(-1/b)^2} = 0 \tag{36}$$

With the limits for both the first and second derivatives known, the limit of the five terms of $f''(x)$ in Eq. (28) simplifies to

$$\lim_{x\Rightarrow 0} f''(x) = \lim_{x\Rightarrow 0}\sum_{j=5}^{9} T_j(x,y) = 4ac(0+b^2+0-1+0) = 4ac(b^2-1) \tag{37}$$

Now Eq. (18) is used to express Eq. (37) in terms of the original variables

$$\lim_{x\Rightarrow 0} f''(x) = 4\left(\frac{\gamma-1}{2}\right)\left(\frac{\gamma}{1-\gamma}\right)\left[\left(\frac{A_\infty}{A_c}\right)^2 - 1\right] = -2\gamma\left[\left(\frac{A_\infty}{A_c}\right)^2 - 1\right] \tag{38}$$

The limit for $f''(x)$ can now be divided by the limit for $g''(x)$ [Eq. (21)] to determine the first term of the Cd_{pre} expression [Eq. (17)],

$$\frac{\lim_{x\Rightarrow 0} f''(x)}{\lim_{x\Rightarrow 0} g''(x)} = \frac{-2\gamma\left[(A_\infty/A_c)^2 - 1\right]}{2\gamma} = 1 - \left(\frac{A_\infty}{A_c}\right)^2 \tag{39}$$

Final Result

This third term limit is then added to the limiting values for the other two terms in Eq. (17) to give

$$Cd_{pre(M_\infty=0)} = 1 - \left(\frac{A_\infty}{A_c}\right)^2 + 2\left(\frac{A_\infty}{A_c}\right)^2 - 2\left(\frac{A_\infty}{A_c}\right) = 1 + \left(\frac{A_\infty}{A_c}\right)^2 - 2\left(\frac{A_\infty}{A_c}\right) = \left(1 - \frac{A_\infty}{A_c}\right)^2 \tag{40}$$

Note that this simple result is independent of the value of γ. This result agrees with the data shown in Fig 9.3 of Ref. 1.

Conclusion

A simple expression, independent of γ, for determining the additive drag coefficient at static conditions has been derived from an existing expression which predicts the additive drag coefficient at non-static conditions.

Acknowledgment

This work was performed as part of a contracted effort to CFD Research Corporation in Huntsville, Alabama. It was submitted for publication with their permission.

Reference

[1] Seddon, J., and Goldsmith, E. L., *Intake Aerodynamics*, 2nd ed., AIAA Education Series, AIAA, Reston, VA, 1999, p. 196.

Intercusp Electron Transport in an NSTAR-Derivative Ion Thruster

John E. Foster*
NASA John H. Glenn Research Center at Lewis Field, Cleveland, Ohio 44135

Introduction

FOR typical magnetic flux densities present in conventional ion thruster discharge chambers, electron motion is influenced by the presence of the magnetic field. In a well-designed ring-cusp discharge chamber, the magnetic field between the magnetic cusps provides a fairly high impedance path for electron flow to the anode, thereby reducing electron losses to intercusp regions.[1] In this respect, it is not surprising that many of the past studies regarding electron transport to the anode in discharge chambers have concentrated on the magnetic cusps where most of the electron current is collected.[1–5] Recently, however, in an effort to save on launch costs as well as to satisfy requirements for smaller spacecraft missions, low-mass ion thrusters are being developed.[6–10] Ion thruster mass reductions can be achieved by reducing the number of magnet rings in the ring-cusp magnetic circuit and by using lightweight, nonmagnetic materials such as aluminum and titanium for discharge chamber construction. The NSTAR ion thruster, which provided the primary propulsion for the Deep Space 1 mission, is an example of such an engine.[11,12] The NSTAR ion thruster featured only three magnet rings and a discharge chamber constructed of titanium and

Received 17 October 2000; revision received 1 March 2001; accepted for publication 18 June 2001.

*Research Scientist, On-Board Propulsion and Power, Ion Group. AIAA Member.

aluminum. The reduction in the number of magnet rings and the use of a nonmagnetic material for the discharge chamber tends to reduce the intercusp magnetic field strength, which in turn gives rise to an increase in electron current to intercusp anode surfaces. Increased electron flow to anode surfaces between the cusps can lead to a lower discharge voltage and, consequently, a reduction in the bulk plasma ionization rate. Under these conditions, the nature of electron flow to intercusp anode surfaces becomes important in thruster operation. In an effort to address this issue, electron diffusion to the anode surfaces between the magnetic cusps was studied in an NSTAR-derivative ion thruster.

Experimental Apparatus

The ion thruster used in this investigation was mechanically identical to the NSTAR thruster. A schematic of the ion thruster and internal discharge chamber wall probes is shown in Fig. 1. A screen grid and accelerator grid comprised the high-voltage ion extraction optics. The voltages at the screen and accelerator grid electrodes (referenced with respect to neutralizer common) ranged from 650 to 1500 V and −250 to −180 V, respectively, as thruster input power varied from 0.5 to 4.6 kW. Thruster discharge power ranged between 120 and 465 W. Additional details regarding the 30-cm engine, the power console, and the propellant feed system may be found elsewhere.[11,12] As can be seen in Fig. 1, the aluminum discharge chamber anode was conical with a downstream cylindrical section. The magnetic circuit consisted of only three permanent magnet rings: 1) the cathode ring, located at the backplate of the conical section; 2) the cylindrical section ring, located at the junction between the cylindrical section and the conical section; and 3) the downstream ring, located at the most downstream flange of the cylindrical section. For these investigations, xenon propellant was used.

Disk-shaped molybdenum wall probes, each with a 6.4-mm-diam collection surface, were used to measure plasma properties at the anode. These planar wall probes were flush mounted with the surface of the anode as indicated in Fig. 1. There was approximately a 1-mm vacuum gap between the edge of the each probe and adjacent anode surfaces. The probes were designated according to the letters as indicated in Fig. 1. Wall probe A was located at the anode near the midpoint between the cathode and cylinder magnetic cusps, and wall probe B was located at the anode near the midpoint between the cylinder and pole piece magnetic cusps. The downstream axial locations of probes A and B with respect to the cathode magnet ring location was 74 and 189 mm, respectively. The magnetic field component parallel to the surface of wall probes A and B was approximately 0.0021 ± 0.0001 and 0.0023 ± 0.0001 T, respectively. The probes were electrically isolated from the anode wall and were held in place using modified compression fittings. The wall probes were biased relative to cathode potential using a variable dc voltage source to obtain langmuir current–voltage characteristics from which plasma density and electron temperature were calculated.

Langmuir Probe Error Analysis

Because the planar probe measurements were made in the environment of the intercusp magnetic field, the analysis of the probes' current–voltage characteristic had to take into account magnetic effects. The magnetic flux at wall probes A and B was primarily parallel to the surface of the probes. Under these conditions, electrons must undergo cross-field diffusion to reach the probe surface. The electron temperature is normally determined from a logarithmic plot of the electron current vs probe voltage in the electron-retarding region of the current–voltage characteristic. The electron temperature is proportional to the reciprocal of the slope of the linear fit to this portion of the plot. In the presence of the magnetic field, the electron current varies more slowly with increasing probe voltage and can yield artificially high electron temperatures. Provided the electron Larmor radius is not less than the probe's sheath thickness (collisionless sheath condition), the electron temperature can still be determined from the probe's current–voltage characteristic. The collisionless sheath condition at probes A and B was satisfied over all of the operation conditions investigated in this work. Under these conditions, if the electron temperature is evaluated over probe bias voltages that are sufficiently negative, the collected electron current dependence on voltage is still described by the thermal Boltzmann factor; therefore, the linear portion of the curve at these negative voltages will provide an accurate measurement of the electron temperature.[13,14] This approach was used to determine the electron temperature from wall probe's current–voltage characteristic in this investigation.

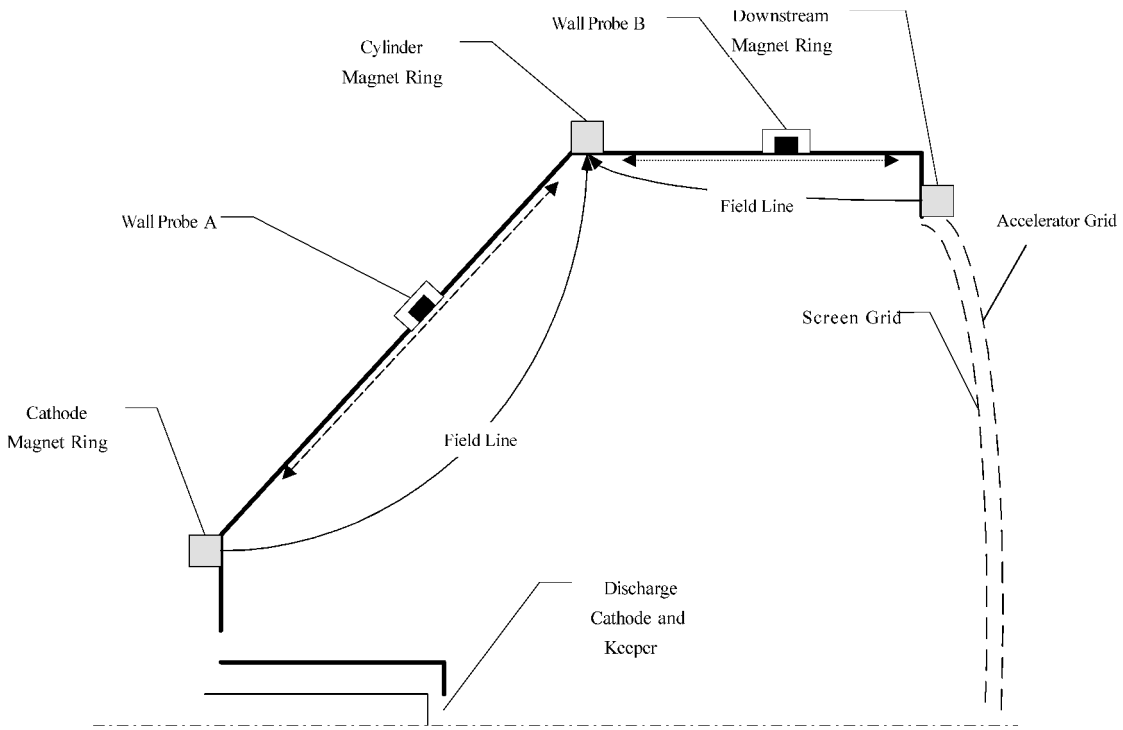

Fig. 1 Half-plane cross-section of NSTAR-derivative thruster revealing wall probes and magnetic circuit; dashed and dotted arrows indicate the line along which Hall probe measurements were made.

The intercusp magnetic field near the probes is not strong enough to affect ion collection appreciably. In this case, the flow of ions to a negatively biased wall probe can be expected to follow the relation

$$\Gamma = 0.61 \cdot e \cdot n_e \cdot \sqrt{k \cdot T_e / M_i} \tag{1}$$

where e is the elementary charge of an electron, n_e is the electron number density, k is the Boltzmann constant, T_e is the electron temperature, and M_i is the ion mass. When Eq. (1) and the determined electron temperature were used, the plasma density at the sheath edge of the probe was determined.

The estimated overall uncertainty in the electron temperature measurement was 15%, whereas the uncertainty in the plasma density was estimated to be between 20 and 25%. Here the uncertainty in the density is determined by sum of the fractional uncertainty in the ion saturation current (15%) and the fractional uncertainty in the square root of the electron temperature (7.5%) (Ref. 15).

In this work, the electron current collected by the probe at and above the plasma potential was calculated and compared to experimentally measured values. This comparison required locating the plasma potential from the experimentally measured current–voltage characteristic. In general, the location of the plasma potential can be determined graphically from a logarithmic plot of the electron current vs the probe voltage. The plasma potential occurs at the intersection (knee) of the electron retarding region and the electron saturation portion of the plot. The knee can be determined by calculating the intersection of a linear fit to the electron retarding region and a linear fit to the electron saturation region for each operating condition. In the presence of the magnetic field, however, this extrapolation technique yields an apparent plasma potential that is lower than the actual value. The magnitude of the plasma potential deviation ΔV_s can be estimated from the formulism derived by Sugawara.[14] The fractional uncertainty in the plasma potential due to the presence of the magnetic field (2–4%) plus the uncertainty in the graphical determination of the plasma potential (1%) yielded a total uncertainty of order 5%. The uncertainty in the location of the plasma potential leads to an average uncertainty in the experimentally determined electron saturation current of approximately 10%.

Results and Discussion

Background

Between the cusps, the magnetic field lines run approximately parallel to the surface of the anode. This field limits the cross-field diffusion of electrons to the anode surface. Figures 2a and 2b show the variation in the measured intercusp magnetic field measured at the anode surface as a function of position relative to the magnetic cusps. The locations of probes A and B are also indicated in Fig. 2. These measurements were made using a Hall probe. The average uncertainty in the magnetic field measurement was approximately 5%, whereas the uncertainty in the Hall probe's position was approximately 2%. The magnetic field in the intercusp region of the conical section of the discharge chamber was normalized to the magnetic field strength measured at probe A. As indicated by the dashed, double-sided arrow in Fig. 1, the magnetic field measurements made at the surface of the conical section were taken with the Hall probe's sensing axis aligned parallel with an imaginary line that included a point at the base of the cone as well as the cone's apex. When the probe is aligned in this manner, it measures the maximum value of the magnetic field component parallel to the surface of the conical section. The magnetic field profile at the anode in the cylindrical section was normalized to the magnetic field intensity measured at wall probe B. The magnetic field measurements made in the cylindrical section were made at the anode surface with the axis of the Hall probe's sensing element lying parallel to the axis of the thruster (see double-sided, dotted arrow in Fig. 1). Again, this orientation allowed for the determination of the maximum value of the field component parallel to the cylindrical section surface. The magnetic cusps are located at positions 0 and 18 cm of Fig. 2a and positions 0 and 12 cm of Fig. 2b. The magnetic field strength drops off rather rapidly as a function of increasing distance from the magnetic cusps. However, as can be seen from Figs. 2, along the anode, at distances greater than 2.5 cm away from the magnetic cusps, the magnetic field does not vary appreciably. As can be seen in Figs. 2, a significant portion of the anode surface lies in these intercusp regions of relatively constant magnetic field. Indeed, over 70% of the anode's surface area lies in these regions of relatively constant magnetic field. Again, the focus of this work is to obtain a better understanding of electron transport to the anode in these regions.

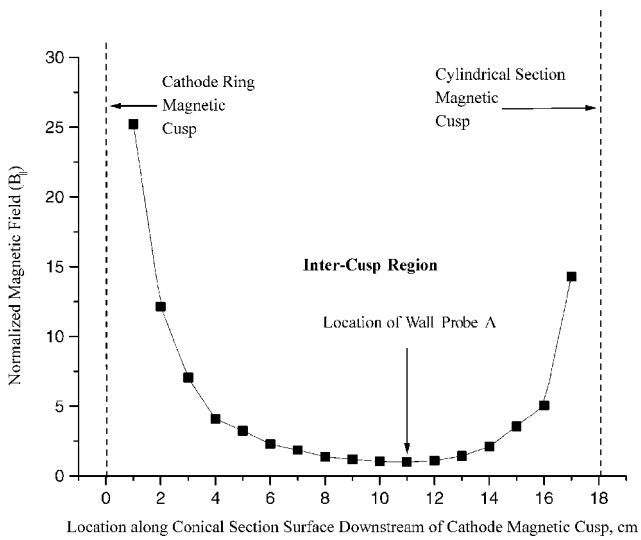

Fig. 2a Normalized intercusp magnetic field along the surface of the conical section.

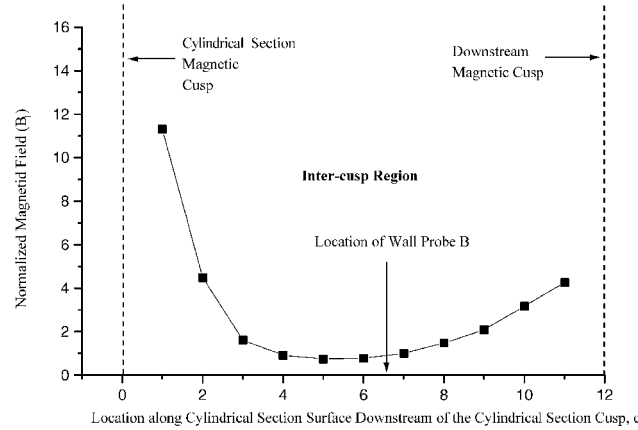

Fig. 2b Normalized intercusp magnetic field along the surface of the cylindrical section.

Electron Transport to Anode Surfaces Between Magnetic Cusps

Ideally, in a ring-cusp discharge chamber, most of the electron current to the anode is collected at the magnetic cusps. In practice, depending on the field strength between the cusps, a significant fraction of the discharge current can be collected at anode surfaces between the cusps. It was found in an earlier NSTAR-derivative thruster study that up to 30% of the discharge current can be collected at anode surfaces between the cusps.[16]

In general, the cross-field flow of electrons to intercusp anode surfaces may be expressed as[17]

$$J_e = -e \cdot \mu \cdot n_e \cdot E_s - e \cdot D_\perp \cdot \frac{\mathrm{d}n_e}{\mathrm{d}r} \tag{2}$$

where μ is the electron mobility, E_s is the electric field, and $D_\perp$ is the cross-field diffusion coefficient. Of interest is the functional behavior of the cross-field diffusion coefficient. In general, plasma flow

across a magnetic field is a complicated problem. Under some conditions, plasma flow obeys classical formulism in which the cross-field diffusion coefficient can be described by

$$D_\perp = D_e \big/ \left[1 + \left(\omega^2 \big/ \nu_e^2\right)\right] \tag{3}$$

where D_e is the electron diffusion coefficient in the absence of a transverse magnetic field, ω is the electron cyclotron frequency, and ν_e is the total electron collision frequency.

Under certain conditions, potential oscillations driven by plasma instabilities give rise to anomalous cross-field diffusion that is substantially larger than classical predictions. In a variety of cases, such anomalous diffusion is best described by the Bohm cross-field diffusion coefficient[17–19]

$$D_\perp = kT_e/16 \cdot e \cdot B \tag{4}$$

where B is the magnetic field component normal to the electron flow. In this work, using Eq. (2) and measured plasma properties at wall probes A and B, the electron current collected at and above plasma potential was calculated as a function of wall probe bias voltage. The total electron collision frequency, which is the sum of the electron–neutral collision frequency and the electron–ion collision frequency, was calculated based on momentum exchange between the Maxwellian electrons at the mean thermal velocity and the background plasma using low energy electron–neutral and electron–ion cross section data.[19] Neutral densities inside the discharge chamber were calculated from the propellant utilization efficiency. The calculation of the electron current was done for two different diffusion coefficients: 1) classical cross-field diffusion coefficient and 2) Bohm cross-field diffusion coefficient. The calculated electron current was then compared with the measured electron current to determine whether classical or Bohm best described electron diffusion to anode surfaces between the magnetic cusps.

To calculate the electron current at the wall probes as a function of probe potential, the electric field at the sheath edge as well as the electron density gradient must be determined. As shown in Fig. 3a, for all cases investigated in this work, the electron current at and above the apparent plasma potential was a linear function of the potential of the probe relative to the plasma potential. The constancy of the slope suggests the notion that the electric field in Eq. (2) is proportional to the potential difference across the sheath. Equation (2) can then be recast,

$$J_e = -e \cdot \mu \cdot n_{e\cdot} \cdot \Delta V \cdot d_{\text{eff}} - e \cdot D_\perp \cdot \frac{\mathrm{d}n_e}{r} \tag{2'}$$

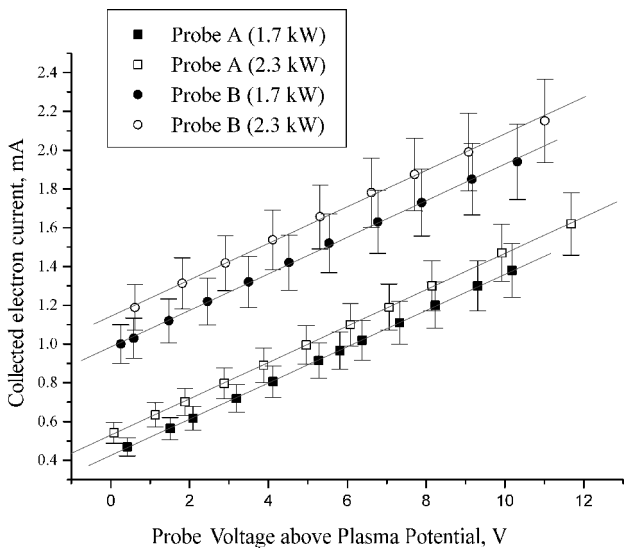

Fig. 3a Electron current collected at wall probes A and B as a function of probe voltage above the plasma potential at different thruster input powers; note the linear variation in electron current with increasing probe voltage.

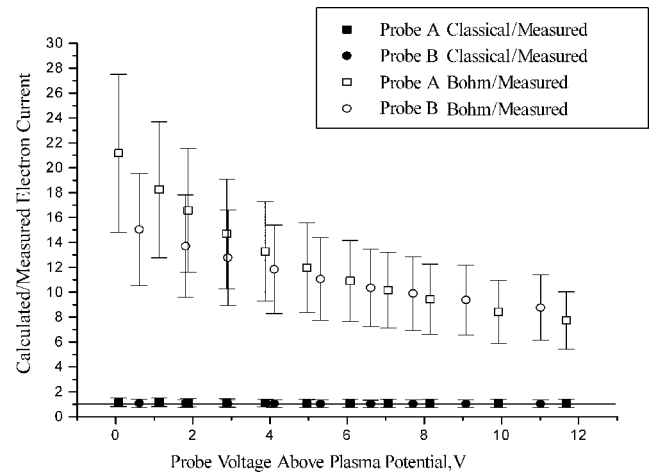

Fig. 3b Comparison between classical and Bohm electron flow to the anode between magnetic cusps at probes A and B (2.3-kW input thruster power).

Here, the electric field at the sheath edge may be expressed as the product of the sheath potential ΔV and the constant of proportionality d_{eff}. The slope of the line described by Eq. (2′), $-e \cdot \mu \cdot n_e \cdot d_{\text{eff}}$, can be obtained from a linear fit (see Fig. 3a). From the slope, d_{eff} can be calculated and, thus, be used to determine the effective electric field at the sheath edge. This effective electric field is a consequence of potentials that leak out of the sheath and give rise to electron drift toward the probe's surface. Such fields cause the collected electron current to increase as a function of increasing sheath potential.

The second term in Eq. (2′) is associated with cross-field diffusion. Classsically, in the presence of the transverse magnetic field, the characteristic diffusion step is a Larmor radius.[17] This scaling provides a simple means for estimating the electron density gradient. The cross-field spatial derivative of the electron density was taken to be the difference between plasma density in the bulk plasma (outside the sheath) and the density at the probe's surface divided by the electron Larmor radius at the probe, (n_e/r_{Le}).

When measured plasma properties and the local magnetic field at each probe were used as inputs, the electron current was determined for both Bohm cross-field diffusion and classical cross-field diffusion. The calculated electron current at each probe was then compared to the measured values. Figure 3b shows the behavior of the ratio of the calculated electron current to the measured electron current as a function of probe voltage for the two wall probes at the 302-W discharge power condition (2.3-kW thruster input power). As can be seen from Fig. 3, the electron collection between the cusps is best described by assuming the classical cross-field diffusion coefficient. To within experimental error (40%), the classical diffusion relation predicted the magnitude of the electron current over a wide discharge power range (200–465 W). Electron current calculated assuming a Bohm cross-field diffusion coefficient was over an order of magnitude larger than that which was measured. Indeed, for the magnetic field intensities present between cusps, if cross-field diffusion were Bohm-like, then the utility of magnetic containment would be defeated due to excessive electron flow to anode surfaces between the magnetic cusps. Note that the classical relation for the electron current also tracked the functional behavior of the electron current with increasing probe voltage. The rate of change in the electron current with increasing probe voltage as calculated using the Bohm diffusion coefficient case was less than that actually measured as evidenced by the monotonically decreasing ratios presented in Fig. 3b.

The suggestion that electron cross-field diffusion to intercusp anode surfaces in the NSTAR-derivative ion thruster is classical implies a number of interesting consequences: 1) Electron diffusion to the anode surface between cusps is severely reduced ($D_\perp \propto 1/B^2$). 2) Because the diffusion is apparently classical, the discharge efficiency penalties associated with reduced intercusp fields in thrusters

with fewer magnet rings or nonmagnetic discharge chambers may not be so great.

Summary

Efforts to reduce thruster mass through the reduction in the number of discharge chamber magnets and the removal of discharge chamber magnetic material can lead to a reduction in the intercusp magnetic field at the anode. Reductions in the containment capability of the intercusp magnetic field could lead to degradation in thruster performance. To address this issue, electron transport to the anode at the intercusp regions was investigated in an NSTAR-derivative ion thruster. Intercusp electron flow to the NSTAR-derivative ion thruster anode as measured at wall probes located between magnetic cusps was found to be classical. Additionally, based on this finding, it should be possible to calculate the magnitude of electron current lost between cusps provided the average magnetic field and local plasma properties between cusps are known.

Acknowledgments

The author would like to thank George Soulas, Michael Patterson, Robert Roman, and James Sovey for assistance in carrying out this work.

Reference

[1]Sovey, J. S., "Improved Ion Containment Using a Ring-Cusp Ion Thruster," *Journal of Spacecraft and Rockets*, Vol. 21, No. 5, 1984, pp. 488–495.

[2]Hershkowitz, N., Leung, K. N., and Romesser, T., "Plasma Leakage Through a Low-Beta Line Cusp," *Physical Review Letters*, Vol. 35, No. 5, 1975, pp. 277–280.

[3]Arakawa, Y., Hamatani, C., and Kawasaki, Y., "Wall Losses of Charge Particles in a Multipole Discharge Plasma," *International Electric Propulsion Conference*, IEPC Paper 84-69, 1989.

[4]Horiike, H., Akiba, M., Ohara, Y., Okumura, Y., and Tanaka, S., "Cusp Width and Power Flow Study at a High Power Magnetic Multipole Source," *Physics of Fluids*, Vol. 30, No. 10, 1987, pp. 3268–3275.

[5]Beattie, J., and Matossian, J., "Mercury Ion Thruster Technology," NASA CR-174974, March 1989, pp. 30–50.

[6]Patterson, M. J., Haag, T. W., and Hovan, S. A., "Performance of the NASA 30 cm Ion Thruster," *International Electric Propulsion Conference*, IEPC Paper 93-108, 1993.

[7]Noci, G., Capacci, M., Redaelli, R., Matucci, A., Matticari, G., Severi, A., and Sabbagh, J., "Development of Small Ion Thrusters for Lightsats Applications," AIAA Paper 95-3071, 10–12 July 1995.

[8]Brophy, J. R., "Advanced Ion Propulsion Technology for Solar System Exploration," AIAA Paper 97-2782, 6–9 July 1997.

[9]Patterson, M. J., and Oleson, S. R., "Low Power Ion Propulsion for Small Spacecraft," AIAA Paper 97-3060, 6–9 July 1997.

[10]Patterson, M. J., "Low-Power Ion Thruster Development Status," AIAA Paper 98-3347, 13–15 July 1998.

[11]Christensen, J. A., Freick, K. J., Hamel, D. J., Hart, S. L., Norenberg, K. T., Haag, T. W., Patterson, M. J., Rawlin, V. K., Sovey, J. S., and Anderson, J. R., "Design and Fabrication of a Flight Model 2.3 kW Ion Thruster for the Deep Space 1 Mission," AIAA Paper 98-3327, 13–15 July 1998.

[12]Sovey, J. S., Hamley, J. A., Haag, T. W., Patterson, M. J., Pencil, E. J., Peterson, T. T., Pinero, L. R., Power, J. L., Rawlin, V. K., Sarmiento, C. J., Anderson, J. R., Bond, T. A., Cardwell, G. I., and Christensen, J. A., "Development of an Ion Thruster and Power Processor for New Millenium's Deep Space 1 Mission," AIAA Paper 97-2778, 6–9 July 1997.

[13]Hutchinson, I. H., *Principles of Plasma Diagnostics*, Cambridge Univ. Press, New York, 1987, pp. 66–71.

[14]Sugawara, M., "Electron Probe Current in a Magnetized Plasma," *Physics of Fluids*, Vol. 9, No. 4, 1966, pp. 797–800.

[15]Taylor, J. R., *An Introduction to Error Analysis*, Oxford Univ. Press, Mill Valley, CA, 1982, pp. 40–80.

[16]Foster, J. E., Soulas, G. C., and Patterson, M. J., "Plume and Discharge Measurements of an NSTAR-Type Ion Thruster," AIAA Paper 2000-3812, 16–19 July 2000.

[17]Chen, F., *Introduction to Plasma Physics and Controlled Fusion*, Plenum, New York, 1984, pp. 169–174, 190–195.

[18]Bohm, D., "Qualitative Description of the Arc Plasma in a Magnetic Field," *The Characteristics of Electrical Discharges in Magnetic Fields*, edited by A. Guthrie and R. K. Wakerling, McGraw–Hill, New York, 1949, pp. 1–12.

[19]Kaufman, H. R., and Robinson, R. S., *Operation of Broad Beam Ion Sources*, Commonwealth Scientific, Alexandria, VA, 1984, pp. 137–141, 142–144.

Optimal Three-Dimensional Nozzle Shape Design Using CFD and Parallel Simulated Annealing

X. Wang* and M. Damodaran†
Nanyang Technological University, Singapore 639798, Republic of Singapore

Introduction

COMPUTATIONAL methods, which are implemented for optimizing aerodynamic shape within the framework of complex single/multidisciplinary optimization design (MDO), are becoming popular in recent years. Most of the current methods of optimization can generally be classified into two distinct groups, namely deterministic and stochastic approaches. Deterministic optimization methods, such as the gradient-based methods and sensitivity analysis, have been favored by many researchers such as Frank et al.[1] One salient feature of gradient-based methods is that they are very efficient in finding the minima of continuously differentiable problems, where sufficiently accurate derivatives can be obtained at reasonable cost. The sensitivity analysis methods have been used in aerodynamic shape design and MDO extensively in recent years; however, sensitivity information cannot be easily extracted from computational fluid dynamics (CFD) codes, and this poses the main obstacle for using gradient-based methods in developing tightly coupled solution methods for MDO. Deterministic methods also largely increase the work of constructing sensitivity analysis models in design problems using CFD. Stochastic optimization methods that are quite robust in searching for the global optimum, such as simulated annealing (SA), genetic algorithm (GA), and genetic simulated annealing (GSA) method, are also being used as nontraditional optimization methods in engineering and scientific research for single and multidisciplinary design optimization. Parallel versions of these algorithms have been extensively applied to solve practical engineering problems for enhancing performance of these approaches and reducing computational overburden in large number of evaluations of the objective function. A survey of parallel simulated annealing (PSA) has been detailed by Aarts and Korst.[2] Further work on these PSA have been done by Diekmann et al.[3] and Gallego et al.[4] Parallel genetic algorithms (PGA) has also attracted attention for its inherent property of parallelization. The basic idea for GA in optimization was introduced by Goldberg.[5] Different forms of implementations of PGA have been outlined by Bianchini and Brown[6] and Cantú-Paz.[7] Doorly et al.[8] have successfully applied a PGA to the problem in aeronautical design optimization. The goal of the present study is to use computational fluid dynamics methods with PSA for global optimization in the design space as described in Wang and Damodaran[9] and in which PSA has been shown to be a suitable tool for reducing wall-clock time for the design of two-dimensional and axisymmetric design problems on coarse-gained processors. In this study the

Received 2 January 2001; revision received 11 June 2001; accepted for publication 3 July 2001.

*Research Fellow, Center for Advanced Numerical Engineering Simulations, Nanyang Avenue. Member AIAA.

†Associate Professor, School of Mechanical and Production Engineering, Center for Advanced Numerical Engineering Simulations, Nanyang Avenue. Senior Member AIAA.